Mapping the spectral phase of isolated attosecond pulses by extreme-ultraviolet emission spectrum

Candong Liu,[1] Zhinan Zeng,[1] Ruxin Li,[1,4] Zhizhan Xu,[1] and Mauro Nisoli[2,3,*]

[1]*State Key Laboratory of High Field Laser Physics, Shanghai Institute of Optics and Fine Mechanics, Chinese Academy of Sciences, Shanghai 201800, China*
[2]*Department of Physics, Politecnico di Milano, Piazza Leonardo da Vinci 32, 20133 Milano, Italy*
[3]*Institute of Photonics and Nanotechnologies, IFN-CNR, Piazza Leonardo da Vinci 32, 20133 Milano, Italy*
[4]*ruxinli@mail.shcnc.ac.cn*
[*]*mauro.nisoli@polimi.it*

Abstract: An all-optical method is proposed for the measurement of the spectral phase of isolated attosecond pulses. The technique is based on the generation of extreme-ultraviolet (XUV) radiation in a gas by the combination of an attosecond pulse and a strong infrared (IR) pulse with controlled electric field. By using a full quantum simulation, we demonstrate that, for particular temporal delays between the two pulses, the IR field can drive back to the parent ions the photoelectrons generated by the attosecond pulse, thus leading to the generation of XUV photons. It is found that the generated XUV spectrum is notably sensitive to the chirp of the attosecond pulse, which can then be reliably retrieved. A classical quantum-path analysis is further used to quantitatively explain the main features exhibited in the XUV emission.

OCIS codes: (020.2649) Strong field laser physics; (190.2620) Harmonic generation and mixing; (320.7110) Ultrafast nonlinear optics.

References and links

1. F. Krausz and M. Ivanov, "Attosecond physics," Rev. Mod. Phys. **81**(1), 163–234 (2009).
2. M. Nisoli and G. Sansone, "New frontiers in attosecond science," Prog. Quantum Electron. **33**(1), 17–59 (2009).
3. M. Chini, K. Zhao, and Z. Chang, "The generation, characterization and applications of broadband isolated attosecond pulses," Nat. Photonics **8**(3), 178–186 (2014).
4. K. T. Kim, D. M. Villeneuve, and P. B. Corkum, "Manipulating quantum paths for novel attosecond measurement methods," Nat. Photonics **8**(3), 187–194 (2014).
5. F. Lépine, M. Y. Ivanov, and M. J. J. Vrakking, "Attosecond molecular dynamics: fact or fiction?" Nat. Photonics **8**(3), 195–204 (2014).
6. F. Krausz and M. I. Stockman, "Attosecond metrology: from electron capture to future signal processing," Nat. Photonics **8**(3), 205–213 (2014).
7. M. Hentschel, R. Kienberger, C. Spielmann, G. A. Reider, N. Milosevic, T. Brabec, P. Corkum, U. Heinzmann, M. Drescher, and F. Krausz, "Attosecond metrology," Nature **414**(6863), 509–513 (2001).
8. P. M. Paul, E. S. Toma, P. Breger, G. Mullot, F. Auge, P. Balcou, H. G. Muller, and P. Agostini, "Observation of a train of attosecond pulses from high harmonic generation," Science **292**(5522), 1689–1692 (2001).
9. A. Scrinzi, M. Geissler, and T. Brabec, "Attosecond cross correlation technique," Phys. Rev. Lett. **86**(3), 412–415 (2001).
10. A. D. Bandrauk, S. Chelkowski, and N. H. Shon, "How to measure the duration of subfemtosecond xuv laser pulses using asymmetric photoionization," Phys. Rev. A **68**(4), 041802 (2003).
11. F. Quéré, J. Itatani, G. L. Yudin, and P. B. Corkum, "Attosecond spectral shearing interferometry," Phys. Rev. Lett. **90**(7), 073902 (2003).
12. J. Itatani, F. Quéré, G. L. Yudin, M. Yu. Ivanov, F. Krausz, and P. B. Corkum, "Attosecond streak camera," Phys. Rev. Lett. **88**(17), 173903 (2002).
13. Y. Mairesse and F. Quéré, "Frequency-resolved optical gating for complete reconstruction of attosecond bursts," Phys. Rev. A **71**(1), 011401 (2005).
14. M. Chini, S. Gilbertson, S. D. Khan, and Z. Chang, "Characterizing ultrabroadband attosecond lasers," Opt. Express **18**(12), 13006–13016 (2010).

#232491 - $15.00 USD Received 16 Jan 2015; revised 1 Apr 2015; accepted 3 Apr 2015; published 9 Apr 2015

15. C. Liu, M. Reduzzi, A. Trabattoni, A. Sunilkumar, A. Dubrouil, F. Calegari, M. Nisoli, and G. Sansone, "Carrier-envelope phase effects of a single attosecond pulse in two-color photoionization," Phys. Rev. Lett. **111**(12), 123901 (2013).
16. E. Cormier, I. A. Walmsley, E. M. Kosik, A. S. Wyatt, L. Corner, and L. F. Dimauro, "Self-referencing, spectrally, or spatially encoded spectral interferometry for the complete characterization of attosecond electromagnetic pulses," Phys. Rev. Lett. **94**(3), 033905 (2005).
17. K. Varjú, Y. Mairesse, P. Agostini, P. Breger, B. Carré, L. J. Frasinski, E. Gustafsson, P. Johnsson, J. Mauritsson, H. Merdji, P. Monchicourt, A. L'Huillier, and P. Salières, "Reconstruction of attosecond pulse trains using an adiabatic phase expansion," Phys. Rev. Lett. **95**(24), 243901 (2005).
18. N. Dudovich, O. Smirnova, J. Levesque, Y. Mairesse, M. Y. Ivanov, D. M. Villeneuve, and P. B. Corkum, "Measuring and controlling the birth of attosecond XUV pulses," Nat. Phys. **2**(11), 781–786 (2006).
19. N. Dudovich, J. Levesque, O. Smirnova, D. Zeidler, D. Comtois, M. Y. Ivanov, D. M. Villeneuve, and P. B. Corkum, "Attosecond temporal gating with elliptically polarized light," Phys. Rev. Lett. **97**(25), 253903 (2006).
20. K. T. Kim, C. Zhang, A. D. Shiner, S. E. Kirkwood, E. Frumker, G. Gariepy, A. Naumov, D. M. Villeneuve, and P. B. Corkum, "Manipulation of quantum paths for space-time characterization of attosecond pulses," Nat. Phys. **9**(3), 159–163 (2013).
21. M. H. Xu, L. Y. Peng, Z. Zhang, Q. Gong, X. M. Tong, E. A. Pronin, and A. F. Starace, "Attosecond streaking in the low-energy region as a probe of rescattering," Phys. Rev. Lett. **107**(18), 183001 (2011).
22. P. Johnsson, R. López-Martens, S. Kazamias, J. Mauritsson, C. Valentin, T. Remetter, K. Varjú, M. B. Gaarde, Y. Mairesse, H. Wabnitz, P. Salières, P. Balcou, K. J. Schafer, and A. L'Huillier, "Attosecond electron wave packet dynamics in strong laser fields," Phys. Rev. Lett. **95**(1), 013001 (2005).
23. P. Johnsson, J. Mauritsson, T. Remetter, A. L'Huillier, and K. J. Schafer, "Attosecond control of ionization by wave-packet interference," Phys. Rev. Lett. **99**(23), 233001 (2007).
24. P. Rivière, O. Uhden, U. Saalmann, and J. M. Rost, "Strong field dynamics with ultrashort electron wave packet replicas," New J. Phys. **11**(5), 053011 (2009).
25. P. Ranitovic, X. M. Tong, B. Gramkow, S. De, B. De Paola, K. P. Singh, W. Cao, M. Magrakvelidze, D. Ray, I. Bocharova, H. Mashiko, A. Sandhu, E. Gagnon, M. M. Murnane, H. C. Kapteyn, I. Litvinyuk, and C. L. Cocke, "IR-assisted ionization of helium by attosecond extreme ultraviolet radiation," New J. Phys. **12**(1), 013008 (2010).
26. M. B. Gaarde, C. Buth, J. L. Tate, and K. J. Schafer, "Transient absorption and reshaping of ultrafast XUV light by laser-dressed helium," Phys. Rev. A **83**(1), 013419 (2011).
27. T. Nakajima and E. Cormier, "Effects of the carrier-envelope phase of chirped laser pulses in the multiphoton ionization regime," Opt. Lett. **32**(19), 2879–2881 (2007).
28. C. Liu, Z. Zeng, R. Li, Z. Xu, and M. Nisoli, "Attosecond photoionization for reconstruction of bound-electron wave packets," Phys. Rev. A **90**(1), 013403 (2014).
29. X. M. Tong and C. D. Lin, "Empirical formula for static field ionization rates of atoms and molecules by lasers in the barrier-suppression regime," J. Phys. At. Mol. Opt. Phys. **38**(15), 2593–2600 (2005).
30. P. B. Corkum, "Plasma perspective on strong field multiphoton ionization," Phys. Rev. Lett. **71**(13), 1994–1997 (1993).
31. K. Kulander, K. J. Schafer, and K. L. Krause, Super-intense laser-atom physics, NATO Advanced Study Institute Series B **316**, 95–110 (1993).
32. K. J. Schafer, M. B. Gaarde, A. Heinrich, J. Biegert, and U. Keller, "Strong field quantum path control using attosecond pulse trains," Phys. Rev. Lett. **92**(2), 023003 (2004).
33. E. Priori, G. Cerullo, M. Nisoli, S. Stagira, S. De Silvestri, P. Villoresi, L. Poletto, P. Ceccherini, C. Altucci, R. Bruzzese, and C. de Lisio, "Nonadiabatic three-dimensional model of high-order harmonic generation in the few-optical-cycle regime," Phys. Rev. A **61**(6), 063801 (2000).
34. C. Liu, R. Li, Z. Zeng, Y. Zheng, P. Liu, and Z. Xu, "Nonadiabatic propagation effect for generating isolated sub-100 as pulses in the high-order harmonic plateau," Opt. Lett. **35**(15), 2618–2620 (2010).
35. J.-H. Kim and C. H. Nam, "Plasma-induced frequency chirp of intense femtosecond lasers and its role in shaping high-order harmonic spectral lines," Phys. Rev. A **65**(3), 033801 (2002).

1. Introduction

In the past decade attosecond science has proven to be a very active research field, with a number of notable applications in atomic, molecular and solid state physics [1, 2]. Ultrafast electron dynamics have been investigated by implementing various novel experimental techniques: attosecond streaking spectroscopy, attosecond transient absorption spectroscopy, attosecond photoemission spectroscopy, based on the measurement of angle-resolved photoelectron or ion spectra, and attosecond nonlinear optics [3–6]. A general prerequisite of any application of ultrashort pulses is the reliable measurement of their temporal characteristics.

Several methods [7–12] have been proposed for the temporal characterization of trains and isolated attosecond pulses (IAPs), usually based on the measurement of the photoelectron

#232491 - $15.00 USD Received 16 Jan 2015; revised 1 Apr 2015; accepted 3 Apr 2015; published 9 Apr 2015

spectra generated by the extreme-ultraviolet (XUV) attosecond pulses in the presence of an infrared (IR) femtosecond field, as a function of the temporal delay between the two pulses. In the following we will focus on IAPs. In this case, the implementation of the attosecond streak camera technique [12], in combination with the Frequency Resolved Optical Gating for Complete Reconstruction of Attosecond Bursts (FROG-CRAB) algorithm [13] allow one to obtain a complete temporal characterization of the streaking IR field and to measure the temporal intensity envelope and spectral phase of the attosecond pulse. Another experimental approach based on the measurement of the photoelectron spectra as a function of the delay between an attosecond and a femtosecond pulse is called Phase Retrieval by Omega Oscillation Filtering (PROOF) [14], which can be used to characterize ultra-broadband attosecond pulses. Both FROG-CRAB and PROOF algorithms do not provide any information about the carrier-envelope phase (CEP) of the attosecond pulses. Recently, it was demonstrated that the CEP of isolated pulses can be obtained by measuring the interference structure in the photoelectron spectra induced by XUV + IR fields [15].

Various all-optical methods, based on the measurement of the spectrum have been proposed and partly implemented to reconstruct the phase of attosecond pulse trains [16–19]. These optical schemes are based on *in situ* measurements, where the production and the measurement of attosecond XUV pulses are entangled. The use of all-optical schemes offers a number of important advantages with respect to the techniques based on the measurement of photoelectrons, in particular a very high detection efficiency and a high signal-to-noise ratio. This is particularly true in the case of high-photon energy attosecond pulses. Recently an *in situ* technique for the measurement of the full space-time structure of the attosecond pulses in the generation medium has been demonstrated [20]. While the *in situ* measurements are extremely useful for the investigation of the physical processes leading to the generation of attosecond pulses, the determination of the temporal characteristics of the pulses in the target region (i.e., in correspondence of the sample under investigation) by using an all-optical technique requires the use of a different approach.

In this work, we propose an all-optical method to characterize the spectral phase of an IAP in the target region. The attosecond pulse to be characterized ionizes an atom and a time-delayed IR pulse with stable CEP is used to steer back to the parent ion the generated electron wave packet. This general scheme has been already investigated by Starace and associates [21] to study the dynamics of low-energy photoelectrons ionized by IAPs in the presence of an intense IR field. Moreover, the use of IR pulses in combination with attosecond pulses in photoemission processes from atoms has been analyzed in the past few years [22–26]. Here we propose a novel scheme, based on the measurement of the spectrum of the XUV photons produced by high-order harmonic generation in a gas by the combined action of an IAP and a strong IR pulse. It is found that the generated spectrum is strongly dependent on both the delay between the two driving pulses and notably on the chirp of the IAP, thus offering an experimental all-optical method for the measurement of the spectral phase of attosecond pulses. The process has been investigated by calculating the numerical solution of the time-dependent Schrödinger equation (TDSE) at the single-atom level, together with considering the on-axis phase-matching effect. The underlying dynamics is understood in terms of the decoupling of the ionization induced by the attosecond pulses and the subsequent electron acceleration controlled by the IR field. The results of the complete numerical model are also discussed in terms of classical electron trajectory analysis.

2. Results and discussion

We consider a linearly chirped Gaussian XUV pulse, whose vector potential is given by the real part of [27, 28]

#232491 - $15.00 USD Received 16 Jan 2015; revised 1 Apr 2015; accepted 3 Apr 2015; published 9 Apr 2015

$$A_{XUV}(t) = -i\frac{1}{\omega_0}\sqrt{\frac{I_0}{\sqrt{1+\xi^2}}}\exp[-i(\omega_0 t+\varphi_0)-2\ln 2\frac{t^2}{\tau^2(1-i\xi)}], \quad (1)$$

where ω_0 is the central carrier frequency, ξ is the dimensionless linear chirp rate controlling the spectral phase of the pulse, φ_0 is the CEP, I_0 and τ are the peak intensity and duration (full width at half maximum) of the transform-limited pulse (ξ = 0), respectively. Equation (1) describes a realistic pulse whose duration and peak intensity depends on the chirp rate, ξ, while its energy and spectral profile do not depend on ξ. The vector potential of the IR pulse is written as

$$A_{IR}(t) = -A_1\cos^2[2\arccos(2^{-1/4})t/T_1]\sin(\omega_1 t+\varphi_1), \quad (2)$$

where A_1 is the peak amplitude, ω_1 is the central carrier frequency, T_1 is the pulse duration, and φ_1 is the CEP. The total vector potential of the two-color driving field is given by $A(t) = A_{IR}(t) + \mathrm{Re}\{A_{XUV}(t - t_d)\}$, where t_d defines the temporal delay between the XUV and IR pulses.

We have calculated the extreme-ultraviolet emission spectrum generated in helium by the two-color laser field by numerical integration of the TDSE within the single-active electron approximation. The numerical solution of TDSE is based on the expansion of the time-dependent wave function in a series of partial waves, which forms a set of coupled equations between the different angular quantum numbers for the radial wave function. The finite-element discrete variable representation (FE-DVR) method is employed to discretize the radial equations with the advantage of providing block-diagonal sparse matrix representation of kinetic operator and the diagonal matrix representation of the effective potential. The temporal evolution of the wave function is carried out by the Arnoldi-Lanczos algorithm. The spectrum is obtained from the Fourier transform of the time-dependent dipole acceleration expectation value, which is calculated via the Ehrenfest theorem using the wave function at each evolution step. The helium atom is described by the effective central potential [29]

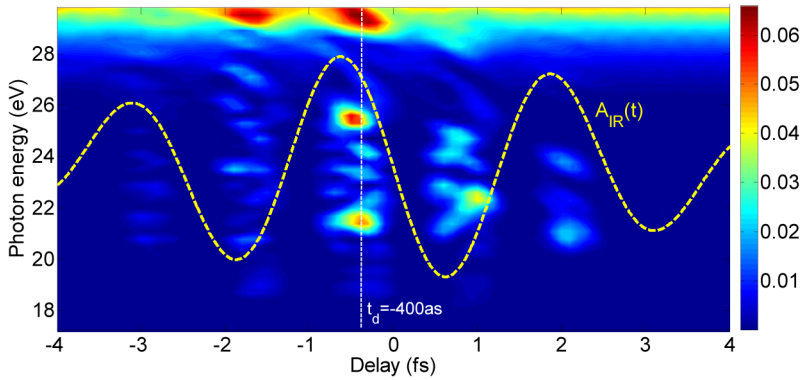

Fig. 1. XUV spectrum generated in helium by the combination of an IR pulse and an isolated attosecond pulse, vs. the temporal delay between the two pulses, calculated by using the full quantum simulations described in the text. The yellow-dashed line is the vector potential of the IR pulse. The parameters of the attosecond pulse used in the simulations are the following: peak intensity $I_0 = 10^{12}$ W/cm^2, transform-limited duration $\tau = 260$ as, central photon energy ω_0 = 36 eV, chirp rate ξ = *0*, and CEP φ_0 = 0. The parameters of the IR pulse used in the simulations are the following: peak intensity $I_1 = 6 \times 10^{13}$ W/cm^2, duration of 5 fs, and central photon energy $\omega_1 = 1.63$ eV (corresponding to a central wavelength of 760 nm).

$$V(r) = -\frac{1.0+1.231e^{-0.662r}-1.325re^{-1.236r}-0.231e^{-0.48r}}{r}. \quad (3)$$

We have first calculated the extreme-ultraviolet spectrum upon scanning the relative delay between the XUV and IR pulses. The parameters of the XUV attosecond pulses are:

#232491 - $15.00 USD Received 16 Jan 2015; revised 1 Apr 2015; accepted 3 Apr 2015; published 9 Apr 2015

transform-limited peak intensity $I_0 = 10^{12}$ W/cm^2, transform-limited duration $\tau = 260$ as, central photon energy $\omega_0 = 36$ eV, chirp rate $\xi = 0$, and CEP value $\varphi_0 = 0$. The parameters of the IR pulse are: peak intensity $I_1 = 6 \times 10^{13}$ W/cm^2, pulse duration 5 fs, and central photon energy $\omega_1 = 1.63$ eV, corresponding to a central wavelength of 760 nm. The simulation parameters used in our calculation are the following: The maximum radial distance is $r_{max} = 300$ a.u. with 600 finite elements and eight basis functions in each element, the maximum angular quantum number is $l_{max} = 10$, the time step of wave function propagation is $\delta t = 0.04$ a.u. and the Arnoldi-Lanczos propagation order is $M = 100$.

The calculated XUV spectra are shown in Fig. 1, as a function of the temporal delay between XUV and IR pulses, in the photon energy range between 18 eV and 30 eV. The yellow-dashed line in Fig. 1 displays the temporal evolution of the IR vector potential. The numerical results clearly show that in the 20-28 eV energy region the XUV radiation is produced only at particular delays around the temporal overlapping region between the two driving pulses. The generation yield shows a notable dependence on the delay: XUV emission is generated in correspondence of the crests of the vector potential of the IR pulse, thus showing a periodic modulation, with a period equal to half-optical cycle of the IR radiation. The origin of the delay-dependent spectrum in Fig. 1 can be understood in terms of the recollision interference picture as follows. For the IR and XUV pulse parameters considered in the simulations, the ionization of the helium atom is mainly governed by the XUV pulse via single-photon excitation, while the IR pulse is only responsible for the control of the electron dynamics in the continuum. Near the crests of the IR vector potential, the IR field results in a momentum shift of the photoelectrons large enough to steer the electronic wave packet back toward the parent ion, where the maximum spatial overlap between the continuum wave packet and the ground state produces efficient continuum-bound transitions thus leading to XUV emission.

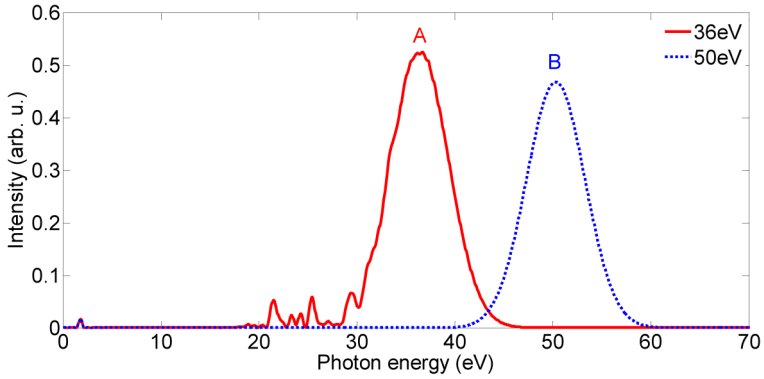

Fig. 2. Comparison of the XUV spectra calculated for the 36-eV (red-solid) and 50-eV (blue-dashed) isolated attosecond pulses at the fixed XUV-IR delay $t_d = -400$ as. Other parameters are the same as in Fig. 1.

To further confirm this interpretation, we have calculated the XUV spectra generated by the two-color field in the case of IAPs with higher central photon energy ($\omega_0 = 50$ eV), without changing the other XUV and IR parameters. The result is shown in Fig. 2. The solid-red line shows the harmonic spectrum generated in the case of IAPs with central energy $\omega_0 = 36$ eV, calculated at a particular delay $t_d = -400$ as; the dashed-blue line represents the harmonic spectrum calculated at the same delay value in the case of IAPs with central energy $\omega_0 = 50$ eV. Here the original IR spectrum used in the simulation has been removed. At low energy (<10 eV) the two spectra representing the rather weak signal are identical, since the emission in this spectral region is generated entirely by the IR pulse, without any contribution from the XUV pulse. In the high-energy region, the Gaussian components A and B shown in

#232491 - $15.00 USD Received 16 Jan 2015; revised 1 Apr 2015; accepted 3 Apr 2015; published 9 Apr 2015

Fig. 2 correspond to the spectra of the IAPs used in the simulations. This can be confirmed by the calculation of the XUV spectra in the absence of the IR pulse. As already shown in Fig. 1, extra emission peaks between 20 and 28 eV, hereafter called recollision emission spectrum (RES), are produced in the case of low-photon energy IAPs, while in the case of high-photon energy IAPs the RES component is not present. The RES absence for high-photon energy excitation supports the proposed recollision interference picture, since the photoelectrons released by 50-eV attosecond pulses are characterized by a higher initial velocity, so that the same IR field is not strong enough to drive the photoelectron back to the parent ion. Thus the tiny continuum-bound overlap inhibits the RES generation.

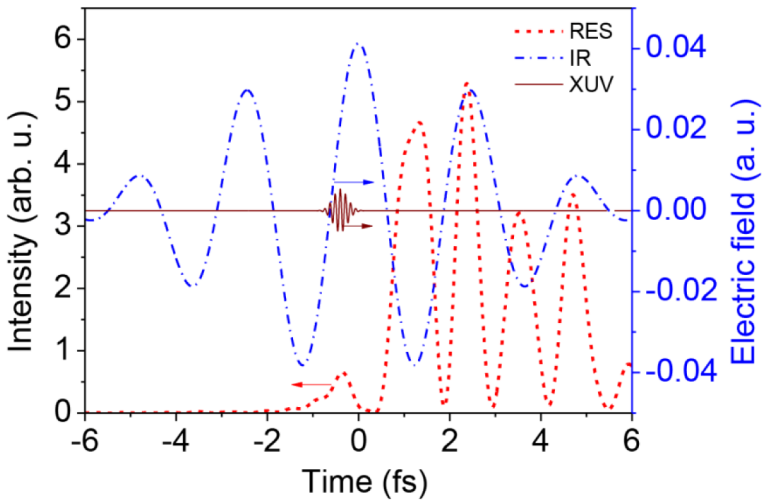

Fig. 3. Temporal intensity profile (red-dashed) of pulse trains corresponding to the RES (20-28 eV), together with the electric field of the IR pulse (blue-dashed-dot) and the XUV pulse (wine-solid) at the XUV-IR delay td = –400 as. Other parameters are the same as in Fig. 1.

A deeper physical insight into the dynamics can be achieved by considering the temporal structure corresponding to the RES. We have employed a square filter to select the RES (20-28 eV) obtained in the case of the XUV-IR delay t_d = –400 as and we have performed the inverse Fourier transform to obtain the temporal intensity profile, as shown by the red-dashed line in Fig. 3, where the driving IR pulse and the XUV pulse are also plotted. A train of pulses is obtained, separated by half-optical cycle of the IR pulse, thus implying multiple recollisions of the electron to the ionic core. Every time the electron passes through the ionic core, an attosecond pulse burst is emitted. This process leads to the harmonic structure of the RES.

It is also possible to analyze the recollision process by calculating the classical electron trajectories in the case of the two-color excitation by using the simple-man model [30, 31], where the first step of tunnel ionization is replaced by the single-photon ionization induced by the attosecond pulse. In this case, the electron released by the absorption of one XUV photon has a nonzero initial velocity v_0, which is estimated as $v_0(t_0) = \pm\sqrt{2[\omega_0 - I_p - V(t_0)]}$ in atomic units [32]. Here, I_p is the ionization energy of the helium atom, and $V(t_0)$ is the height of the Coulomb barrier combined with the IR field at the release moment t_0. The positive and negative velocity values correspond to electrons released in two opposite directions, thus forming two families of classical electron trajectories. The harmonic emission is associated with the maximum continuum-bound overlap described by those trajectories where

#232491 - $15.00 USD Received 16 Jan 2015; revised 1 Apr 2015; accepted 3 Apr 2015; published 9 Apr 2015

$$[v_0 - A_{IR}(t_0)](t_f - t_0) + \int_{t_0}^{t_f} A_{IR}(t')\,dt' = 0\,, \tag{4}$$

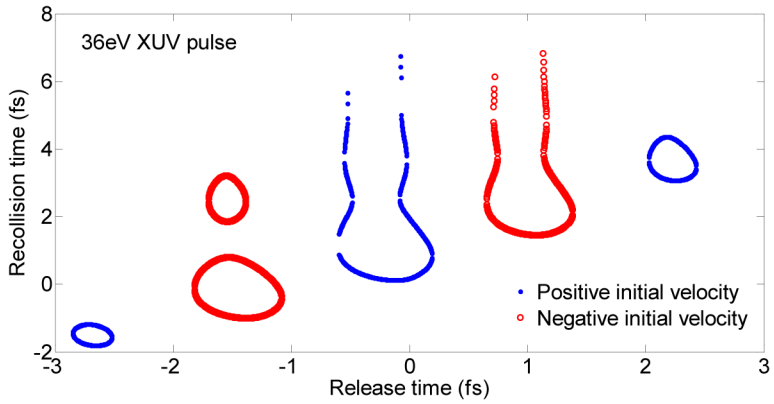

Fig. 4. Classical electron trajectories characterized by a pair of release time and recollision time. Blue dots and red cycles represent the positive and negative initial velocity used in the classical electron trajectory analysis, respectively. The XUV and IR pulse parameters are the same as in Fig. 1.

which corresponds to electrons that, under the action of the IR field, can return to the ionic core at the recollision instant, t_f. The solution of Eq. (4) in the case of 36-eV pulses yields two families of trajectories, as shown in Fig. 4, which displays all the possible returning trajectories characterized by the release time and the recollision time in the case of positive (blue-dot) and negative (red-cycle) velocity values, v_0. Figure 4 shows that a given release time may correspond to more than one recollision times, in agreement with the multiple recollision picture. These trajectories can form five branches of harmonic generation, in which consecutive branches correspond to the two different trajectory families. We can see that the number and position of these branches agree well with the TDSE result reported in Fig. 1. We have then applied the classical model in the case of IAPs centered at 50 eV. In this case no returning electron trajectories exist, thus explaining the absence of the extra harmonic emission, as previously discussed. We point out that when the electron returns to the ionic core, it will leave the ionic core with non-zero velocity by scattering from the ionic potential [21]. This process is different from the well-known three-step model of high harmonic generation, where the electron recombines with the parent ion at the last step. Consequently, in our parameter regime, the harmonic photon energy cannot be simply expressed as the sum of the electron kinetic energy obtained in the external field and the atomic ionization potential.

A notable result of our numerical calculations is that the high harmonic generation process induced by the two-color field encodes the spectral phase information of the attosecond pulse. This is due to the fact that the ionization step is determined by single-photon ionization, which makes the spectrum of the XUV pulse be directly mapped onto the free electron wave packet that finally interferes with the atomic ground state. Figure 5(a) shows the harmonic spectrum calculated assuming an XUV-IR delay of –400 as, for three different chirp rates of the 36-eV attosecond pulse: (i) $\xi = 0$, (ii) $\xi = 2$, and (iii) $\xi = -2$. As we have already discussed, the harmonic spectra reported in Fig. 5(a) below 10 eV and above 30 eV are generated independently by the IR pulse and by the XUV pulse, respectively, and are not affected by the chirp of the XUV pulse. On the contrary, the RES spectral components between 20 and 30 eV strongly depend on the chirp of the attosecond pulse. This offers the possibility to measure the XUV spectral phase using an all-optical method. Figure 5(b) shows the RES calculated at t_d = –400 as upon changing the chirp in the range $-3 \le \xi \le 3$.

#232491 - $15.00 USD Received 16 Jan 2015; revised 1 Apr 2015; accepted 3 Apr 2015; published 9 Apr 2015

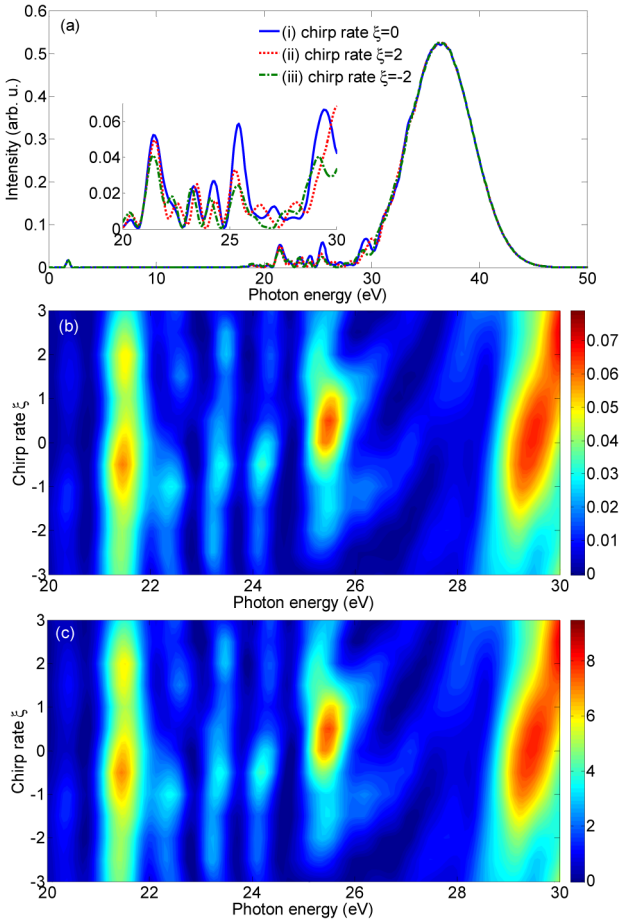

Fig. 5. (a) Comparison of the XUV spectrum calculated at the fixed XUV-IR delay t_d = –400 as for three different chirp rates of the XUV pulse: ξ = 0, (ii) ξ = 2, and (iii) ξ = –2. Inset is a zoom of the spectra in the region between 20 and 30 eV. (b) Singe-atom RES versus chirp rates of the XUV pulse at the fixed XUV-IR delay t_d = –400 as. (c) Macroscopic on-axis RES versus chirp rates of the XUV pulse at the fixed XUV-IR delay t_d = –400 as. Other parameters are the same as in Fig. 1.

It is well-known that macroscopic propagation effects play an important role in high harmonic generation [33, 34]. The full simulation of the macroscopic RES generated in the XUV + IR fields requires the numerical solution of Maxwell propagation equation with the source term of the single-atom response obtained by the TDSE. In order to make the simulation manageable and reveal the essential physical picture, we have used a simple one-dimensional (1D) wave equation to consider the macroscopic RES along the propagation axis, while the single-atom response is still calculated by numerically solving three-dimensional (3D) TDSE. We can arrange that the IR pulse is loosely focused so that the on-axis intensity variation and the phase deviation from the plane wave due to focusing effect can be neglected. The focusing effect of the XUV pulse along the propagation axis is taken into account by modifying Eq. (1) as [35]

$$A_{XUV}^{(f)}(z,t) = \frac{A_{XUV}(t - z/c)}{\sqrt{1 + (z/z_0)^2}} \exp[-i \arctan(z/z_0)], \tag{5}$$

#232491 - $15.00 USD Received 16 Jan 2015; revised 1 Apr 2015; accepted 3 Apr 2015; published 9 Apr 2015

where z is the position coordinate, z_0 is the Rayleigh length, and c is the light speed. The total vector potential of the two-color field along the propagation axis is therefore given by $A(z,t) = A_{IR}(t - z/c) + \mathrm{Re}\{A_{XUV}^{(f)}(z, t - t_d)\}$. We assume an XUV pulse with a 20-μm beam waist, corresponding to a Rayleigh length of z_0 = 36.4 mm at 36 eV, is focused at the entrance of 1-mm-thick gas cell filled with 10-torr gas pressure. By integrating the 1D wave equation, we can obtain the macroscopic on-axis RES calculated at $t_d = -400$ as upon changing the chirp in the range $-3 \le \xi \le 3$, as shown in Fig. 5(c). The comparison of Fig. 5(b) and 5(c) demonstrates that the chirp-dependent RES structure is nearly not modified by the on-axis propagation effect. An almost one-to-one mapping relation between chirp and RES shape is visible. In other words, the RES produced by XUV pulses with different chirp are also different, so that it is possible to retrieve a unique chirp value from the RES structure. We note that, from the experimental point of view, the measurement of the XUV-IR temporal delay can be affected by a relative uncertainty. However, we can still implement a procedure to determine the XUV chirp rate. We denote the experimental RES as $I(t_e, \omega)$, where t_e is the measured XUV-IR delay, and the calculated RES as $S(t_d, \omega, \xi)$, where t_d is the exact XUV-IR delay. The experimental delay, t_e, can be calibrated to the exact value t_d by shifting the temporal axis: $t_d = t_e + t_c$, where t_c is a time constant. The two unknown parameters (ξ, t_c) can be determined by searching the optimal values that minimize the root-mean-square error between the two-dimensional normalized data $I(t_d - t_c, \omega)$ and $S(t_d, \omega, \xi)$. The minimization technique can be implemented by the algorithm of Simulated annealing which has given good results in avoiding local minima. The time cost for the retrieval procedure is mainly dependent on the calculation of the single-atom TDSE which usually needs several hours using parallel code.

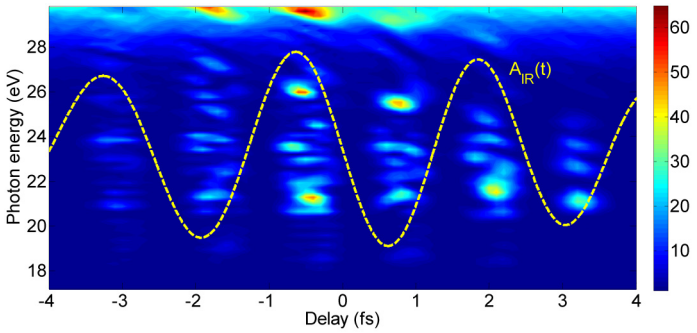

Fig. 6. The RES generated in helium by the combination of a chirped IR pulse and an isolated attosecond pulse, vs. the temporal delay between the two pulses. The yellow-dashed line is the vector potential of the chirped IR pulse. The chirp rate of the IR pulse is set to 1, leading to a broadening of the pulse duration from 5 fs to 7 fs. Other simulation parameters are the same as in Fig. 1.

We have analyzed the effect of the chirp of the IR pulse on the RES structures. The RES is calculated for a chirped IR pulse used in combination with an isolated attosecond pulse, upon scanning the temporal delay between the two pulses. The result is shown in Fig. 6, where the yellow-dashed line displays the temporal evolution of the chirped IR vector potential. Apart from the chirp of the IR pulse, which leads to a broadening of the pulse duration from the transform-limited value of 5 fs to 7 fs, the other parameters of the simulation are the same as in Fig. 1. We note that the IR chirp affects the shape of the RES structures, so that, in order to characterize the chirp rate of the attosecond pulses, the IR chirp has to be independently measured (*e.g.*, by using the frequency resolved optical gating method).

#232491 - $15.00 USD Received 16 Jan 2015; revised 1 Apr 2015; accepted 3 Apr 2015; published 9 Apr 2015

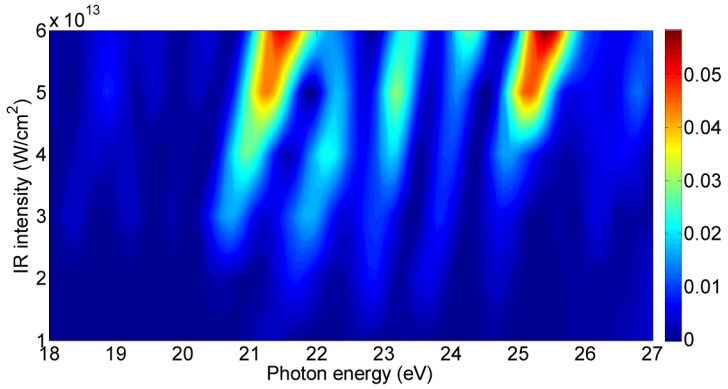

Fig. 7. Singe-atom RES versus the intensity of the chirp-free IR pulse at the fixed XUV-IR delay t_d = –400 as. Other simulation parameters are the same as in Fig. 1.

We have then calculated the influence of the IR intensity on the RES in the single-atom response. Figure 7 shows the RES in energy region between 18 eV and 27 eV as a function of the IR intensity at a fixed XUV-IR delay t_d = –400 as. Apart from scanning the IR intensity, other simulation parameters are the same as in Fig. 1. As the IR intensity is decreased, we can clearly see a linear shift of the RES energy position towards the low-energy direction together with the reduced RES intensity. When the IR intensity decreases to 10^{13}W/cm^2, the IR field cannot steer the photoelectron induced by XUV pulse to ionic core so that the RES finally disappears. Since the IR intensity affects position and shape of the RES, in order to characterize the chirp rate of the attosecond pulses such intensity has to be independently measured.

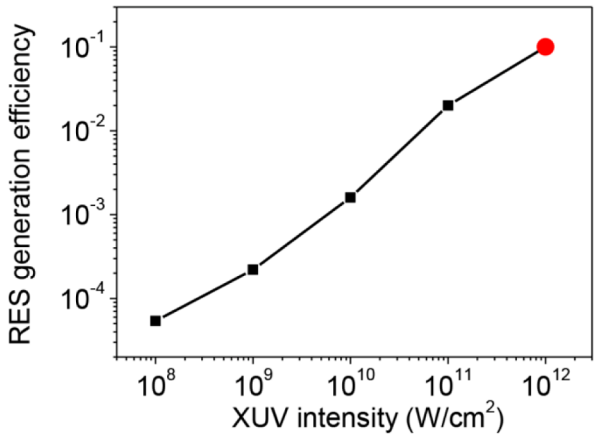

Fig. 8. RES generation efficiency as a function of the XUV pulse intensity, calculated at the fixed XUV-IR delay t_d = –400 as. Other simulation parameters are the same as in Fig. 1. The point corresponding to the XUV intensity used in Fig. 1 is shown as a red filled circle.

Efficient generation of the RES requires a good temporal and spatial overlap between the IR and the XUV pulses. The spot size in the beam waist of the IR and XUV pulses can be reasonably assumed as 150 μm and 20 μm, respectively. In the above discussion, the peak intensity of the IR pulse is set as $I_1 = 6 \times 10^{13}$ W/cm^2. In this case, the intensity of the IR beam at the radial position corresponding to the radial edge of the XUV beam can be approximately estimated as $I_2 = I_1 \exp(-20/150) \approx 5.25 \times 10^{13}$ W/cm^2. At this IR intensity (I_2), we can see from Fig. 7 that the RES structure is only slightly changed, which does not significantly affect the retrieval procedure. Upon increasing the IR spot size and upon

#232491 - $15.00 USD Received 16 Jan 2015; revised 1 Apr 2015; accepted 3 Apr 2015; published 9 Apr 2015

increasing the XUV spot size, the effect of the IR intensity variation along the radial profile could be further reduced.

Another important issue is the estimation of the efficiency of the RES generation. We have calculated the RES generation efficiency, which is defined as the ratio between the maximum amplitude of the RES and the intensity of the main XUV spectrum at 36 eV, upon scanning the XUV pulse intensity for a fixed XUV-IR delay $t_d = -400$ as. The result is shown in Fig. 8, which shows an almost linear dependence of the efficiency vs. the XUV intensity over a wide range from 10^8 to 10^{12} W/cm^2.

The crucial point for the all-optical measurement is to steer the continuum electron wave packet to revisit the parent core. This can be achieved by either increasing the peak intensity of the IR pulse or using longer wavelengths. In order to characterize high-photon energy XUV pulses, the use of long-wavelength IR radiation presents a number of important advantages. As an example, we consider an XUV pulse with central photon energy $\omega_0 = 150$ eV and transform-limited duration 60 as, and an IR pulse with photon energy $\omega_1 = 0.69$ eV (central wavelength 1800 nm), peak intensity 6×10^{14} W/cm^2 and duration 12 fs. In this case the simulation parameters used in our calculation are the following: the maximum radial distance is $r_{max} = 500$ a.u. with 1000 finite elements and eight basis functions in each element, the maximum angular quantum number is $l_{max} = 30$, the time step of wave function propagation is $\delta t = 0.04$ a.u. and the Arnoldi-Lanczos propagation order is $M = 330$. The calculated chirp-dependent RES at the fixed XUV-IR delay $t_d = -400$ as is shown in Fig. 9, where for the sake of clarity, we plot only the spectral region between 118 eV and 122 eV. Our result demonstrates that the proposed all-optical method is also applicable in the characterization of the chirp rate of high-photon energy attosecond pulses.

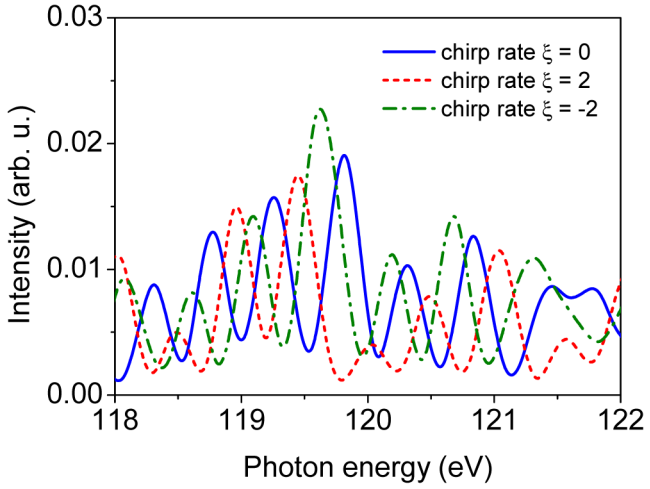

Fig. 9. Comparison of the RES calculated at the fixed XUV-IR delay $t_d = -400$ as for three different chirp rates of the XUV pulse: $\xi = 0$, $\xi = 2$, and $\xi = -2$. The parameters used in the simulations are the following. XUV pulse: transform-limited duration $\tau = 60$ as, central photon energy $\omega_0 = 150$ eV. IR pulse: peak intensity 6×10^{14} W/cm^2, duration 12 fs, photon energy $\omega_1 = 0.69$ eV (wavelength 1800 nm).

The evaluation of the influence of transient absorption on the macroscopic RES is a very challenging task, beyond the scopes of this work. We used a relatively simple method to estimate the absorption degree of the RES. We calculated the IR-dressed absorption cross section of single Helium atom using the method described by Gaarde *et al.* [26]. In the calculation, the model potential of Eq. (3) is used and the IR pulse parameters are the same as in Fig. 2. The Beer's law was employed to evaluate the macroscopic absorption degree. We note that, for the particular experiment parameters assumed in this work (low gas pressure

#232491 - $15.00 USD Received 16 Jan 2015; revised 1 Apr 2015; accepted 3 Apr 2015; published 9 Apr 2015

and short length of the gas cell), single-atom effects are the predominant ones, so that 3D propagation effects can be reasonably neglected. Figure 10 shows the calculated RES (green line) upon considering the effect of absorption in the case of a 1-mm-thick gas cell with a10-torr gas pressure, together with the original RES (red line), extracted from Fig. 2, for 36-eV attosecond pulses. The absorption is not uniform over the RES: around 21.4 eV it is about 4%, it increases up to about 50% between 22 eV and 26 eV and then decreases to about 25% in the energy range between 26 eV and 45 eV. Figure 10 clearly shows that absorption affects the relative height and the width of the peaks lying in the RES. Therefore, for a correct application of the reconstruction procedure described in this work, the IR-dressed gas transmission curve has to be considered in order to reproduce the experimental results.

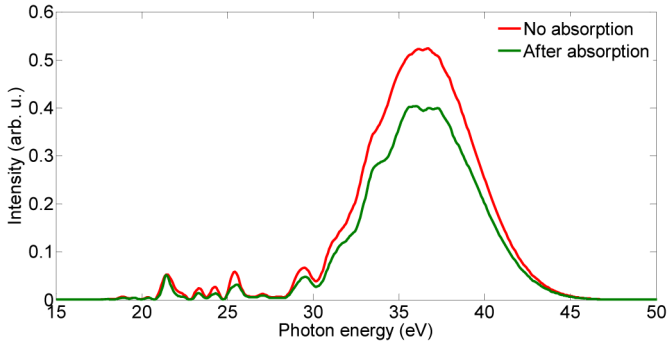

Fig. 10. Comparison of the original RES (red line) extracted from Fig. 2 and the RES (green line) calculated from Beer's law upon taking into account the absorption effect.

3. Conclusion

In conclusion, we have discussed a novel all-optical method for the measurement of the spectral phase of isolated attosecond pulses, based on the use of a two-color scheme. A CEP-stable IR pulse is employed to drive back to the parent ions some of the photoelectrons generated by the IAP in a gas medium. The XUV spectrum generated by the two-color field is notably sensitive to the chirp of the attosecond pulse, which can thus be uniquely determined. A full quantum simulation has been performed to demonstrate the potentialities of the technique. A simple classical electron trajectory description, in very good agreement with the quantum simulations, has been discussed to obtain a clear physical picture of the processes at the basis of the proposed measurement technique.

Acknowledgments

This work was supported by the National Natural Science Foundation of China (Grants No. 11127901, No. 61221064, No. 11404356), 973 Project (Grant No. 2011CB808103), Shanghai Commission of Science and Technology Yangfan Project (Grant No. 14YF1406000), Shanghai Institute of Optics and Fine Mechanics Specialized Research Fund (Grant No. 1401561J00) and the European Research Council under the European Community's Seventh Framework Programme (FP7/2007-2013)/ERC Grant Agreement No. 227355 ELYCHE.

#232491 - $15.00 USD Received 16 Jan 2015; revised 1 Apr 2015; accepted 3 Apr 2015; published 9 Apr 2015